

Experimental demonstration of quantum optimal control via the alternating control-evolution protocol

Ruiqi Tang(汤睿琪), Yanjun Hou(侯彦君), Zhenyue Du(杜臻越), Zhuoyue Xu(徐卓越), Yuquan Chen(陈昱全), Zhaokai Li(李兆凯), and Xinhua Peng(彭新华)

Citation: Chin. Phys. B, 2026, 35 (**6**): 060302. DOI: 10.1088/1674-1056/ae56e0
http://cpb.iphy.ac.cn; http://iopscience.iop.org/cpb

What follows is a list of articles you may be interested in

Observation of topology of non-Hermitian systems without chiral symmetry

Shuo Wang(王硕), Zhengjie Kang(康正杰), Hao Li(李浩), Jiaojiao Li(李姣姣), Yuanjie Zhang(张元杰), and Zhihuang Luo(罗智煌)

Chin. Phys. B, 2025, 34 (**11**): 110304. DOI: 10.1088/1674-1056/addcc1

Micron-resolved quantum precision measurement of magnetic field at the Tesla level

Si-Han An(安思瀚), Shi-Yu Ge(葛仕宇), Wen-Tao Lu(卢文韬), Guo-Bin Chen(陈国彬), Sheng-Kai Xia(夏圣开), Ai-Qing Chen(陈爱庆), Cheng-Kun Wang(王成坤), Lin-Yan Yu(虞林嫣), Zhi-Qiang Zhang(张致强), Yang Wang(汪洋), Gui-Jin Tang(唐贵进), Hua-Fu Cheng(程华富), and Guan-Xiang Du(杜关祥)

Chin. Phys. B, 2024, 33 (**12**): 120305. DOI: 10.1088/1674-1056/ad7e9b

New approach to measuring topological phase transitions utilizing Floquet technology

Xue-Ying Yang(杨雪滢), Wei Wu(吴伟), and Ping-Xing Chen(陈平形)

Chin. Phys. B, 2024, 33 (**9**): 090305. DOI: 10.1088/1674-1056/ad5d94

Approximate constructions of counterdiabatic driving with NMR quantum systems

Hui Zhou(周辉), Xiaoli Dai(代晓莉), Jianpei Geng(耿建培), Yunlan Ji(季云兰), and Xinhua Peng(彭新华)

Chin. Phys. B, 2024, 33 (**9**): 090301. DOI: 10.1088/1674-1056/ad58b2

Nuclear magnetic resonance for quantum computing: Techniques and recent achievements

Tao Xin(辛涛), Bi-Xue Wang(王碧雪), Ke-Ren Li(李可仁), Xiang-Yu Kong(孔祥宇), Shi-Jie Wei(魏世杰), Tao Wang(王涛), Dong Ruan(阮东), Gui-Lu Long(龙桂鲁)

Chin. Phys. B, 2018, 27 (**2**): 020308. DOI: 10.1088/1674-1056/27/2/020308

RAPID COMMUNICATION

Experimental demonstration of quantum optimal control via the alternating control–evolution protocol

Ruiqi Tang(汤睿琪)[1], Yanjun Hou(侯彦君)[1], Zhenyue Du(杜臻越)[1], Zhuoyue Xu(徐卓越)[1], Yuquan Chen(陈昱全)[1,†], Zhaokai Li(李兆凯)[1,2,3,‡], and Xinhua Peng(彭新华)[1,2,3]

[1] *Laboratory of Spin Magnetic Resonance, School of Physical Sciences, Anhui Province Key Laboratory of Scientific Instrument Development and Application, University of Science and Technology of China, Hefei* 230026, *China*

[2] *Hefei National Research Center for Physical Sciences at the Microscale, University of Science and Technology of China, Hefei* 230026, *China*

[3] *Hefei National Laboratory, University of Science and Technology of China, Hefei* 230088, *China*

(Received 8 January 2026; revised manuscript received 15 March 2026; accepted manuscript online 25 March 2026)

As a crucial component of quantum technologies, quantum optimal control enables the high-fidelity engineering of desired quantum states and operations. Conventional approaches, such as the widely used gradient ascent pulse engineering (GRAPE) algorithm, typically rely on dense pulse sequences with a large number of control parameters, leading to inefficient optimization and increased sensitivity to experimental imperfections. In this work, we propose the alternating control–evolution (ACE) protocol, a flexible framework that constructs quantum operations by interleaving elementary control operations with tunable free evolutions, thereby enabling the design of sparse pulse sequences that exploit intrinsic system dynamics. This design substantially reduces the number of control parameters while retaining high expressibility and control fidelity. Numerical simulations on nuclear magnetic resonance systems show that the ACE protocol achieves more than a 20-fold reduction in the number of control parameters compared to GRAPE, with comparable fidelity in state preparation tasks. We further experimentally validate the ACE protocol on a four-qubit NMR platform by preparing a Greenberger–Horne–Zeilinger (GHZ) state with a fidelity of 99.52%. These results demonstrate that the ACE protocol provides an efficient and experimentally robust strategy for quantum optimal control, particularly suitable for the noisy intermediate-scale quantum (NISQ) era.

Keywords: quantum optimal control, nuclear magnetic resonance, quantum state preparation

PACS: 03.67.Ac, 76.60.–k

DOI: 10.1088/1674-1056/ae56e0 **CSTR:** 32038.14.CPB.ae56e0

1. Introduction

Quantum optimal control aims to determine time-dependent control parameters that steer the dynamics of a specific quantum system towards a desired target with high accuracy, such as a specific quantum state or a unitary operation.[1–3] Over the past few decades, quantum optimal control has become a powerful experimental tool and is adopted in extensive applications for advancing quantum technologies,[4–6] including quantum simulation, quantum sensing, and the development of scalable quantum computational devices.[7–9] Various optimization methods have been developed, such as gradient ascent pulse engineering (GRAPE)[10,11] and its variants,[12,13] the stochastic gradient descent (SGD) method,[14] the Krotov method,[15,16] the chopped random basis (CRAB) method,[17,18] and diffusion models.[19] Among these, methods based on a large number of successive, discretized control pulse slices have been particularly successful and have been implemented across various experimental platforms, such as superconducting quantum circuits,[20] circuit QED,[21,22] trapped ions,[23,24] and nuclear magnetic resonance systems.[25] While such dense parametrization provides strong expressive power, it also introduces significant practical challenges. The large number of control parameters leads to a high-dimensional optimization parameter landscape, resulting in high computational overhead and reduced optimization efficiency. In experiments, long sequences of successive control pulse slices tend to amplify the accumulation of systematic errors and are susceptible to hardware imperfections such as finite bandwidth[26] and pulse distortions,[27,28] therefore limiting the accuracy of control operations. These issues motivate the development of novel control strategies capable of achieving comparable performance with a reduced number of control parameters.

In this work, we introduce the alternating control–evolution (ACE) protocol, a flexible framework for gradient-based quantum optimal control. The key idea of the ACE protocol is to construct the quantum operation by interleaving two elements: control pulse slices and tunable free evolutions, thereby enabling the exploitation of the intrinsic dynam-

†Corresponding author. E-mail: yuquanchen@ustc.edu.cn

‡Corresponding author. E-mail: zkli@ustc.edu.cn

© 2026 Chinese Physical Society and IOP Publishing Ltd. All rights, including for text and data mining, AI training, and similar technologies, are reserved.

ics of the quantum system. This protocol enables the design of sparse pulse sequences with a reduced number of control parameters while retaining high expressibility and controllability. To verify the effectiveness of the ACE protocol, we first conduct numerical simulations of Haar-random quantum state preparation using parameters derived from a realistic nuclear magnetic resonance (NMR) quantum processor. Our results show that by leveraging the natural evolution of the quantum system, the ACE protocol reduces the number of control parameters to 5% of that used in the conventional method while maintaining high control fidelity. As a result, the ACE protocol consistently outperforms the conventional GRAPE algorithm in both optimization efficiency and robustness against noise. Furthermore, we experimentally demonstrate the feasibility of the ACE protocol by preparing a Greenberger–Horne–Zeilinger (GHZ) state on a 4-qubit NMR platform using sparse pulse sequences generated by ACE, achieving an experimental fidelity of 99.52%. These numerical and experimental results demonstrate that the ACE protocol offers an efficient and experimentally robust strategy for quantum optimal control, which is particularly suitable in the noisy intermediate-scale quantum (NISQ) era.

2. Alternating control–evolution protocol

We begin by formulating the quantum state engineering problem. The dynamics of a quantum system are governed by a Hamiltonian that can be decomposed into natural system evolution and external control components:

$$H(t) = H_{\rm sys} + H_{\rm ctrl}(t), \tag{1}$$

where $H_{\rm sys}$ denotes the natural Hamiltonian dynamics determined by the specific physical system. The control Hamiltonian, arising from time-varying external fields, takes the form

$$H_{\rm ctrl}(t) = \sum_{\alpha} u_{\alpha}(t) H_{\alpha}, \tag{2}$$

where the index α denotes the components of the Hamiltonian, and H_{α} represents the Hamiltonian term associated with the control field of amplitude $u_{\alpha}(t)$. For notational convenience, we define the control vector $\boldsymbol{u}(t)$ as the collection of all control amplitudes $\{u_{\alpha}(t)\}$.

In the problem of closed system state engineering, the objective is to identify the optimal control parameters $\boldsymbol{u}(t)$ that transfer an initial state $|\psi_{\rm in}\rangle$ (e.g., $|0\rangle^{\otimes n}$) to a target state $|\Psi\rangle$, under a given total evolution time T. Formally, this state transfer task can be cast as a quantum optimal control problem.[10] The infidelity serves as the cost function

$$L = 1 - \left|\langle\Psi|U_{\rm total}|\psi_{\rm in}\rangle\right|^2, \tag{3}$$

which quantifies the distance between the current operation and the target. Here $U_{\rm total}$ denotes the total evolution operator obtained by solving the Schrödinger equation:

$$\dot{U}(t) = -{\rm i}H(t)U(t), \quad U(0) = I^{\otimes n}, \tag{4}$$

evaluated at $t = T$.

To solve this problem, various approaches are employed, which typically rely on dense pulse sequences with a large number of control parameters. The gradient ascent pulse engineering (GRAPE) algorithm is a widely used method to design such control pulse sequences.[10] Throughout this paper, GRAPE refers to the conventional implementation using dense pulse sequences. The large number of control parameters results in a high-dimensional optimization parameter space, which introduces drawbacks both computationally and experimentally. On the computational side, the abundance of variables results in parameter redundancy, which decreases optimization efficiency. On the experimental side, the use of successive control pulse slices amplifies the accumulation of systematic errors and can cause undesirable effects, such as adverse heating effects[29] and increased sensitivity to finite bandwidth[18,26] and pulse distortion[27,28] in practical systems.

2.1. Design of the protocol

To address this issue, we propose the ACE protocol for quantum optimal control. As illustrated in Fig. 1, our protocol is constructed from three fundamental components:

1. An elementary control operation;
2. Free evolution governed by the system Hamiltonian;
3. Gradient-based optimization of control parameters.

The joint integration of these three components, as illustrated in Fig. 1, provides an efficient framework for solving quantum optimal control problems.

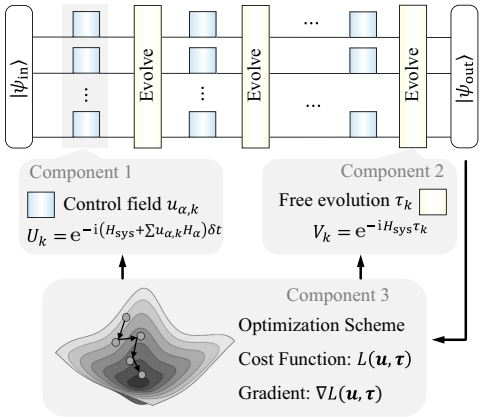


Fig. 1. The alternating control–evolution protocol. The protocol is based on a layered structure consisting of alternating elementary control operations $u_{\alpha,k}$ and free evolution periods τ_k. The $|\psi_{\rm in}\rangle$ is the initial state, and $|\psi_{\rm out}\rangle$ is the output state. The infidelity between the output state $|\psi_{\rm out}\rangle$ and the target state $|\Psi\rangle$ serves as the cost function $L(\boldsymbol{u},\boldsymbol{\tau})$. The parameters $u_{\alpha,k}$ and τ_k are optimized through gradient descent to minimize the cost function $L(\boldsymbol{u},\boldsymbol{\tau})$, transferring the initial state $|\psi_{\rm in}\rangle$ to the target state $|\Psi\rangle$.

The first component is a short pulse slice of a fixed duration δt, implementing a constant control amplitude within the slice. Specifically, we use the control vector $\boldsymbol{u}_k$ to denote the set of control amplitudes in the k-th layer $\{u_{\alpha,k}\}_{\alpha=1,2,\ldots}$, where $u_{\alpha,k}$ represents the control amplitude associated with the Hamiltonian term H_α in the k-th layer. The control amplitudes $\boldsymbol{u}_k$ in the k-th layer generate the temporal-evolution control propagator

$$U_k(\boldsymbol{u}_k) = \exp\left[-\mathrm{i}\left(H_{\mathrm{sys}} + \sum_\alpha u_{\alpha,k} H_\alpha\right)\delta t\right]. \tag{5}$$

The physical implementation of these elementary control operations is platform-dependent, offering broad applicability. For instance, they correspond to laser pulses addressing individual ions or atoms in trapped-ion[23,24,30] or neutral-atom systems.[31,32] In superconducting quantum circuits, they are typically achieved via microwave pulses applied to transmon qubits.[20,33] In NMR systems[10] and nitrogen–vacancy (NV) centers,[34,35] radio frequency (RF) pulses act as the elementary control operations.

The second component introduces free evolution with variable durations $\boldsymbol{\tau}$, which is the key point of the ACE protocol. Here τ_k denotes the free evolution duration in the k-th layer under the system Hamiltonian H_{sys}. For the k-th layer, the temporal-evolution free-evolution propagator is given by

$$V_k(\tau_k) = \exp\left(-\mathrm{i}H_{\mathrm{sys}}\tau_k\right). \tag{6}$$

This component is universally applicable across quantum platforms, as every quantum system possesses intrinsic dynamics H_{sys} that can be leveraged. The intrinsic system dynamics can generate coherent interactions, such as correlations and entanglement, which can be harnessed to achieve quantum optimal control with less external control overhead.

The first two components combine to form the alternating control–evolution structure that defines the ACE protocol. By alternating between applying elementary control operations and free-evolution periods, we create a sequence of K control–evolution layers, where each layer consists of a control operation followed by a free-evolution period. The natural Hamiltonian dynamics H_{sys} generate quantum correlations at a slower timescale, while external control fields enable faster and direct operations. Therefore, alternating these two approaches yields a superior strategy for quantum control.

Let $U_{k_2:k_1}$ denote the composite propagator from layer k_1 through layer k_2 (for $k_1 \le k_2$):

$$U_{k_2:k_1} = V_{k_2}U_{k_2}\cdots V_{k_1}U_{k_1}. \tag{7}$$

We set $\boldsymbol{u} = \{\boldsymbol{u}_k\}_{k=1,2,\ldots,K}$ to represent all control amplitudes of all the K layers and $\boldsymbol{\tau} = \{\tau_k\}_{k=1,2,\ldots,K}$ to represent the free evolution durations of all K layers. The adjustable parameters to be optimized are the control amplitudes $\boldsymbol{u}$ and free evolution durations $\boldsymbol{\tau}$, forming a combined parameter space $(\boldsymbol{u},\boldsymbol{\tau})$. The total unitary evolution over the complete sequence of K layers is then given by

$$U_{\mathrm{total}}(\boldsymbol{u},\boldsymbol{\tau}) = V_K(\tau_K)U_K(\boldsymbol{u}_K)\cdots V_1(\tau_1)U_1(\boldsymbol{u}_1) = U_{K:1}. \tag{8}$$

The third component provides the parameter update rule for the above control sequences. Specific formulas will be derived in the next subsection.

The ACE protocol offers a generalized perspective on quantum control sequence design. The GRAPE approach, which uses long sequences with successive control pulse slices, can be viewed as a limiting case of the ACE protocol, where all free evolution durations are constrained to zero ($\tau_k = 0$). In this limit, the control pulses are applied without interruption. In contrast, the ACE protocol inherently facilitates sparse pulse sequence design, which allocates the majority of the total evolution time T to free evolution periods, thereby enabling the use of fewer control parameters. In Section 3, numerical comparisons will be made through state preparation tasks with GRAPE.

2.2. Gradient for the cost function

The third component is the optimization process that tailors the protocol for the quantum optimal control task. The optimization parameters of the ACE protocol are the control amplitudes $\boldsymbol{u}$ and the free evolution durations $\boldsymbol{\tau}$, defining the total unitary evolution $U_{\mathrm{total}}(\boldsymbol{u},\boldsymbol{\tau})$. By applying the total unitary evolution $U_{\mathrm{total}}(\boldsymbol{u},\boldsymbol{\tau})$ to Eq. (3), the cost function can be written as

$$L(\boldsymbol{u},\boldsymbol{\tau}) = 1 - |\langle\Psi|V_K(\tau_K)U_K(\boldsymbol{u}_K)\cdots V_1(\tau_1)U_1(\boldsymbol{u}_1)|\psi_{\mathrm{in}}\rangle|^2, \tag{9}$$

aiming to transfer the initial state $|\psi_{\mathrm{in}}\rangle$ to the target state $|\Psi\rangle$. Here, $\boldsymbol{u}_k = \{u_{\alpha,k}\}_{\alpha=1,2,\ldots}$ represents the set of all control amplitudes in the k-th layer. To find the specific solution $(\boldsymbol{u}^*,\boldsymbol{\tau}^*)$, the gradient components of the ACE protocol can be computed as

$$\begin{aligned}\frac{\partial L(\boldsymbol{u},\boldsymbol{\tau})}{\partial u_{\alpha,k}} &= 2\,\mathrm{Re}(\lambda\langle\Psi|\mathrm{i}\delta t\cdot U_{\mathrm{left}}V_kH_\alpha U_kU'_{\mathrm{right}}|\psi_{\mathrm{in}}\rangle),\\ \frac{\partial L(\boldsymbol{u},\boldsymbol{\tau})}{\partial \tau_k} &= 2\,\mathrm{Re}(\lambda\langle\Psi|\mathrm{i}\cdot U_{\mathrm{left}}H_{\mathrm{sys}}U_{\mathrm{right}}|\psi_{\mathrm{in}}\rangle).\end{aligned} \tag{10}$$

The coefficient λ is given as

$$\lambda = \langle\psi_{\mathrm{in}}|U_{K:1}^\dagger|\Psi\rangle. \tag{11}$$

The left and right operators are given as

$$\begin{aligned}U_{\mathrm{left}} &= U_{K:k+1},\\ U_{\mathrm{right}} &= U_{k:1},\\ U'_{\mathrm{right}} &= U_{k-1:1}.\end{aligned} \tag{12}$$

After calculating the gradient $\nabla L(\boldsymbol{u},\boldsymbol{\tau})$ for the cost function, the parameters can be adjusted by the update rule:

$$u_{\alpha,k} \leftarrow u_{\alpha,k} - \gamma \frac{\partial L}{\partial u_{\alpha,k}},$$
$$\tau_k \leftarrow \tau_k - \gamma \frac{\partial L}{\partial \tau_k}. \tag{13}$$

The flexibility of the ACE protocol extends to its optimization strategies. For instance, we implement a two-stage approach: initially optimizing control parameters $\boldsymbol{u}$ with fixed evolution durations $\boldsymbol{\tau}$, then performing joint optimization of both parameter types within a localized region.

3. Adaptation to NMR quantum systems

Having established the ACE protocol framework, we now demonstrate its performance through application to the NMR system, a well-established platform for quantum control experiments. An NMR system consists of an ensemble of nuclear spins that are manipulated through transverse, time-varying magnetic fields.[36] Using Pauli operators $\{\hat{\sigma}_x, \hat{\sigma}_y, \hat{\sigma}_z\}$, the Hamiltonian can be expressed as

$$H_{\mathrm{NMR}} = \sum_{j=1}^{n} \left(\pi \nu_j \hat{\sigma}_z^{(j)}\right) + \sum_{i<j}^{n} \left(\frac{\pi}{2} J_{ij} \hat{\sigma}_z^{(i)} \hat{\sigma}_z^{(j)}\right),$$
$$H_{\mathrm{ctrl}}(t) = \sum_{j=1}^{n} \left(\pi u_{2j-1}(t) \hat{\sigma}_x^{(j)} + \pi u_{2j}(t) \hat{\sigma}_y^{(j)}\right). \tag{14}$$

Here H_{NMR} is the system Hamiltonian, ν_j denotes the precession frequency of the j-th spin, and J_{ij} represents the scalar coupling strength between spins i and j. The parameters of the system Hamiltonian H_{NMR} depend on the structure of the samples used. Specific values for the samples used in this work are provided in Appendix B.

The $H_{\mathrm{ctrl}}(t)$ is the control Hamiltonian; the amplitude $u_\alpha(t)$ mentioned in Eq. (2) refers to $u_{2j-1}(t)$ and $u_{2j}(t)$, which are associated with the radio-frequency (RF) pulses along the x and y directions. Therefore, the j-th spin is manipulated with RF pulses $u_{2j-1}(t)$ and $u_{2j}(t)$, respectively. The control vector $\boldsymbol{u}(t) = \{u_j(t)\}_{j=1,\ldots,2n}$ contains a total of $2n$ control parameters to be optimized.

A crucial constraint in NMR systems arises from homonuclear spins: spins belonging to the same nuclear species share identical control fields, i.e., $u_{2i-1}(t) = u_{2j-1}(t)$ and $u_{2i}(t) = u_{2j}(t)$ for homonuclear spins i and j. Consequently, the effective degrees of freedom for quantum control in NMR are determined by the number of nuclear species rather than the number of individual qubits, presenting a challenge for control algorithm design.

In the NMR implementation of the ACE protocol, the elementary control operation for the k-th layer takes the form of a controlled RF pulse. This pulse is characterized by control amplitudes $u_{\alpha,k}$ and has a short, fixed duration δt. The free evolution of the second component is governed by the system Hamiltonian H_{NMR} and characterized by variable durations τ_k. Consequently, each controlled RF pulse is followed by a free evolution period, forming the layered control–evolution sequence of the ACE protocol. For a sequence containing K such layers, the total unitary evolution U_{total} is computed according to Eq. (8). To optimize the layered control–evolution sequence, we construct the cost function $L(\boldsymbol{u},\boldsymbol{\tau})$ as a function of the control amplitudes $\{u_{\alpha,k}\}$ and evolution durations $\{\tau_k\}$. The optimization proceeds by computing both the cost function and its gradient $\nabla L(\boldsymbol{u},\boldsymbol{\tau})$, which guide the parameter updates according to the framework described in Subsection 2.2. The cost function $L(\boldsymbol{u},\boldsymbol{\tau})$ and the gradient components

$$\nabla L(\boldsymbol{u},\boldsymbol{\tau}) = \left(\frac{\partial L}{\partial u_{\alpha,k}}, \frac{\partial L}{\partial \tau_k}\right) \tag{15}$$

are derived from Eqs. (3) and (10). Through iterative gradient-based optimization, we can minimize $L(\boldsymbol{u},\boldsymbol{\tau})$ to achieve high-fidelity state transfer from the initial state $|\psi_{\mathrm{in}}\rangle$ to the target state $|\Psi\rangle$. Let N_{nuclear} represent the number of nuclear species, as spins of the same type must be addressed collectively. For a sequence containing K such layers, the number of control parameters to be optimized can be written as $K(2N_{\mathrm{nuclear}}+1)$, as there are $2N_{\mathrm{nuclear}}$ control amplitudes and 1 free evolution duration for each layer.

The constrained layering approach of the ACE protocol naturally leads to sparse pulse sequences with fewer control parameters. The following numerical simulation shows that these sparse sequences can achieve high-fidelity state preparation, exhibiting enhanced optimization efficiency along with robustness against noise.

3.1. Expressibility of ACE protocol

We conducted a prior test to investigate the effectiveness of the ACE protocol, which employs sparse pulse sequences for optimization with fewer parameters. A critical factor influencing this performance is the expressibility, defined as the ability to generate states that can effectively explore the Hilbert space.[37–39]

Mathematically, our protocol can be described by a parameterized unitary ensemble $U(\boldsymbol{u},\boldsymbol{\tau})$. Through the unitary ensemble, we can obtain the corresponding state ensemble

$$\mathcal{E}_{\mathrm{frame}} = \{\psi(\boldsymbol{u},\boldsymbol{\tau}) | \psi(\boldsymbol{u},\boldsymbol{\tau}) = U(\boldsymbol{u},\boldsymbol{\tau})|\psi_{\mathrm{in}}\rangle\} \tag{16}$$

from a fixed reference state $|\psi_{\mathrm{in}}\rangle$ (typically $|\psi_{\mathrm{in}}\rangle = |0\rangle^{\otimes n}$). The expressibility can be quantified by measuring the deviation between the statistical distribution of $\mathcal{E}_{\mathrm{frame}}$ and the ideal uniform distribution (i.e., the ensemble of Haar-random states).[40] A smaller deviation indicates a higher expressibility, meaning

that the protocol can generate states that cover the Hilbert space more uniformly.

There exists a numerical method that can be employed to evaluate this deviation.[41] We sample a number of parameter vectors $\{(\boldsymbol{u}_i, \boldsymbol{\tau}_i)\}$ uniformly from the allowed space $(\boldsymbol{u}, \boldsymbol{\tau})$ to generate a state ensemble $\mathcal{E}_{\text{frame}}$. We then compute the overlap $O = |\langle\psi(\boldsymbol{u}_i, \boldsymbol{\tau}_i)|\psi(\boldsymbol{u}_j, \boldsymbol{\tau}_j)\rangle|^2$ for each pair of states from this ensemble, thereby constructing an estimated overlap distribution $\hat{P}_{\text{frame}}(O)$. This distribution is compared with the ideal probability density function of state overlaps for Haar-random states:[42]

$$P_{\text{Haar}}(O) = (N-1)(1-O)^{N-2}. \tag{17}$$

Here O corresponds to the state overlap, and $N = 2^n$ is the dimension of the Hilbert space. The deviation between the two distributions is measured using the Kullback–Leibler (KL) divergence:[43]

$$D_{\text{KL}}\left(P_{\text{Haar}} \middle\| \hat{P}_{\text{frame}}\right) = \sum_O P_{\text{Haar}}(O) \cdot \log \frac{P_{\text{Haar}}(O)}{\hat{P}_{\text{frame}}(O)}. \tag{18}$$

Here $\hat{P}_{\text{frame}}$ is the estimated probability distribution of state overlaps generated from the ACE protocol, and $D_{\text{KL}}\left(P_{\text{Haar}} \middle\| \hat{P}_{\text{frame}}\right)$ is used to quantify the discrepancy involved in approximating the ideal distribution P_{Haar} with the estimated model $\hat{P}_{\text{frame}}$ in our ACE protocol. A smaller D_{KL} value indicates a closer statistical agreement with the Haar distribution, implying higher expressibility.

We assessed the expressibility of the ACE protocol across various system sizes and different control–evolution layers on NMR platforms. It can be seen that the KL divergence exhibits a decreasing trend with the increasing number of control–evolution layers across all investigated systems in Fig. 2(a). According to previous studies,[41] a structure achieves high expressibility when the KL divergence reaches 10^{-3}, which generates quantum states with a nearly uniform distribution in the Hilbert space. As illustrated in Fig. 2(a), our ACE protocol reaches a superior KL divergence of 10^{-4} with fewer than 100 layers across all system sizes, demonstrating a high expressibility. The number of layers increases modestly with the system size. Furthermore, Fig. 2(b) shows the estimated overlap distribution $\hat{P}_{\text{frame}}(O)$ at two different KL divergence values. The results further demonstrate that the estimated overlap distribution $\hat{P}_{\text{frame}}(O)$ closely matches the theoretical Haar distribution $P_{\text{Haar}}(O)$ at a KL divergence of 10^{-4}, at which point the statistical properties of the state ensemble $\mathcal{E}_{\text{frame}}$ approach those of the ideal Haar-random ensemble. These results suggest that the ACE protocol exhibits high expressibility with sparse pulse sequences, implying its potential for state preparation tasks.

3.2. Scalability and robustness for state preparation

After evaluating the expressibility, we apply the ACE protocol to state preparation tasks and proceed to investigate its practical performance, including computational scalability and robustness compared with the GRAPE algorithm.

To assess scalability, we conducted numerical simulations on systems ranging from 2 to 7 qubits for Haar-random state preparation.[44] For each system size, 500 distinct target states were generated. The task was to transfer the fixed initial state $|0\rangle^{\otimes n}$ to each target state using both the ACE protocol and the GRAPE algorithm. The optimization was carried out using the L-BFGS-B algorithm.[45] Unlike the expressibility test, which sampled the full parameter space $(\boldsymbol{u}, \boldsymbol{\tau})$, the free-evolution durations τ_k for each layer in the ACE protocol were fixed to a constant value τ in the test of scalability and robustness to enable a direct comparison with the GRAPE algorithm. This means only the first-stage optimization in ACE was utilized, optimizing only the control pulse parameters $\{u_{\alpha,k}\}$ to reach the same target fidelity as GRAPE. Therefore, the total evolution time T_{ACE} of the ACE protocol with K control–evolution layers is given by $T_{\text{ACE}} = K(\delta t + \tau)$, and the total number of control parameters to be optimized is $K \times 2N_{\text{nuclear}}$. For the GRAPE algorithm with M control pulse slices of fixed duration Δt, the total evolution time is $T_{\text{GRAPE}} = M\Delta t$, and the total number of control parameters is $M \times 2N_{\text{nuclear}}$. Under a fixed total time constraint $T_{\text{ACE}} = T_{\text{GRAPE}} = T$, an appropriate number of layers K was chosen through prior tests to allow the optimizer to converge to the fidelity threshold. Subsequently, with the control slice duration δt fixed, the corresponding τ is determined by the relation $\tau = T/K - \delta t$; detailed information can be found in Appendix A.

Our results show that the ACE protocol achieves successful convergence with a fidelity of 99.7%, utilizing sparse pulse sequences with $10 \sim 100$ control–evolution layers across the tested 2-qubit to 7-qubit systems. The total number of control parameters to be optimized is $(10 \sim 100) \times 2N_{\text{nuclear}}$. In contrast, under an identical total evolution time T and fidelity requirement, the GRAPE algorithm uses $500 \sim 2700$ control pulse slices. The total number of control parameters to be optimized is $(500 \sim 2700) \times 2N_{\text{nuclear}}$. Our ACE protocol achieves more than a 20-fold reduction in the number of control parameters compared to GRAPE. It is worth mentioning that the GRAPE algorithm fails to converge when constrained to the same number of control parameters as the ACE protocol. Therefore, the ACE protocol exhibits superior parameter efficiency compared to the GRAPE algorithm. Figure 2(c) shows the runtime for preparing the random states across different NMR system sizes for both methods. It can be seen that the ACE protocol (represented by blue dots) exhibits a stable speedup trend compared to the GRAPE algorithm (represented by red dots). Specifically, the speedup factor is observed to

be over 20 times across the tested system sizes, demonstrating an improvement in optimization efficiency. Due to the excessive runtime of the GRAPE algorithm for the seven-qubit case, twenty-five random states are prepared in the seven-qubit simulation for GRAPE. The results reveal that employing our ACE protocol to design sparse pulse sequences enables high-fidelity optimal control with fewer parameters, which outperforms the GRAPE algorithm in optimization efficiency.

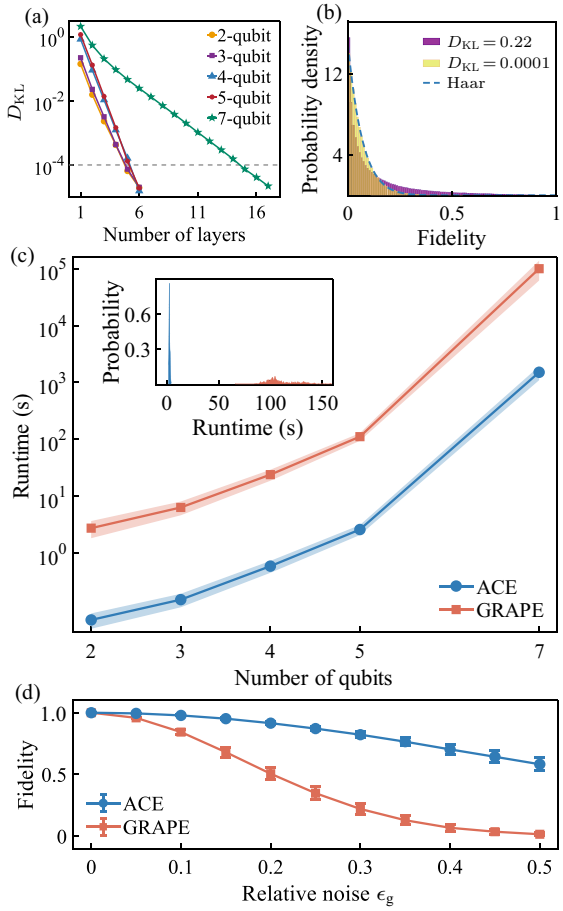


Fig.2 . Benchmark of the ACE protocol for state preparation on NMR quantum systems compared to the GRAPE algorithm. (a) A semi-log plot showing the KL divergence between the estimated overlap distributions generated by the ACE protocol with different numbers of layers and the ideal Haar distribution. (b) The comparison of the estimated overlap distributions generated by the ACE protocol at different KL divergences ($D_{KL} = 0.22$ of layer $K = 1$ and $D_{KL} = 10^{-4}$ of layer $K = 5$) against the Haar distribution curve for the 4-qubit case. (c) A semi-log plot showing the runtime for optimization varying with the increasing system size of both methods. Each point represents an average runtime of successfully preparing 500 random target states on a given size NMR system with a fidelity of 99.7%. The colored band-region accounts for the standard deviation across trials. The inset displays the runtime probability distribution for the 5-qubit case. (d) The average fidelity versus the relative amplitude of Gaussian noise. Each point represents the average fidelity from 500 randomly generated Gaussian noise signals with the same relative amplitude applied to the control sequence. The colored error bar indicates the standard deviation across trials.

Furthermore, we numerically assessed the robustness of both methods by perturbing the optimized control sequences with Gaussian noise of different amplitude ϵ_g and evaluating the resulting fidelity loss. The total evolution of the perturbed pulse sequence can be expressed as $U(\boldsymbol{u}', \boldsymbol{\tau})$, which is influenced by the relative noise amplitude ϵ_g. The control amplitudes $\boldsymbol{u}'$ under perturbation can be written as

$$u'_{\alpha,k} = (1 + \epsilon_g \eta_{\alpha,k}) u_{\alpha,k}, \quad \eta_{\alpha,k} \sim \mathcal{N}(0,1). \tag{19}$$

With the free evolution durations fixed, the noisy evolution $U(\boldsymbol{u}', \boldsymbol{\tau})$ can be computed using the perturbed control amplitudes $\boldsymbol{u}'$ according to Eq. (8). In contrast, the total evolution of the pulse sequence without noise is denoted by $U(\boldsymbol{u}, \boldsymbol{\tau})$, corresponding to the case $\epsilon_g = 0$. The impact of the noise is quantified by the fidelity between the noisy evolution $U(\boldsymbol{u}', \boldsymbol{\tau})$ and the ideal evolution $U(\boldsymbol{u}, \boldsymbol{\tau})$, given by

$$F(U(\boldsymbol{u}, \boldsymbol{\tau}), U(\boldsymbol{u}', \boldsymbol{\tau})) = \frac{\left|\mathrm{Tr}(U(\boldsymbol{u}, \boldsymbol{\tau})^\dagger \cdot U(\boldsymbol{u}', \boldsymbol{\tau}))\right|^2}{d^2}, \tag{20}$$

where $d = 2^n$ is the dimension of the Hilbert space. A higher fidelity indicates a smaller accuracy loss caused by the noise, thus signifying better robustness of the control sequence. The results in Fig. 2(d) show that the ACE protocol (represented by blue dots) maintains higher fidelity across the whole tested noise spectrum in contrast to the GRAPE algorithm (represented by red dots). This demonstrates that the ACE protocol exhibits enhanced robustness against control field imperfections.

Overall, by designing a suitably sparse pulse sequence with the ACE protocol, we can achieve high-fidelity state preparation with fewer parameters. Such sparse pulse sequences yield higher optimization efficiency and enhanced robustness against noise for quantum optimal control tasks.

4. Experimental verification

Following the numerical demonstrations of the ACE protocol's superior performance, we experimentally validate the protocol through GHZ state preparation on a 4-qubit NMR system. The experiment utilizes a sample of ^{13}C-iodotrifluoroethylene dissolved in d-chloroform. The sample comprises one ^{13}C and three ^{19}F nuclear spins, which can serve as four qubits (see Appendix B for detailed molecular structure and Hamiltonian parameters).[46,47] Due to the homonuclear nature of the three fluorine (^{19}F) spins, they share a common control channel, which constrains the RF pulses applied to this channel to have identical amplitudes. Consequently, the Hamiltonian can be expressed as

$$\begin{aligned} H_{\mathrm{NMR}} &= \sum_{j=1}^{4} \left(\pi \nu_j \hat{\sigma}_z^{(j)}\right) + \sum_{i<j}^{4} \left(\frac{\pi}{2} J_{ij} \hat{\sigma}_z^{(i)} \hat{\sigma}_z^{(j)}\right), \\ H_{\mathrm{ctrl}}(t) &= \pi u_1(t) \hat{\sigma}_x^{(1)} + \pi u_2(t) \hat{\sigma}_y^{(1)} \\ &\quad + \pi u_3(t) (\hat{\sigma}_x^{(2)} + \hat{\sigma}_x^{(3)} + \hat{\sigma}_x^{(4)}) \\ &\quad + \pi u_4(t) (\hat{\sigma}_y^{(2)} + \hat{\sigma}_y^{(3)} + \hat{\sigma}_y^{(4)}). \end{aligned} \tag{21}$$

H_{NMR} is the system Hamiltonian and $H_{\mathrm{ctrl}}(t)$ is the control Hamiltonian. The k-th layer consists of an elementary control pulse parameterized by four amplitudes $\{u_{1,k}, u_{2,k}, u_{3,k}, u_{4,k}\}$

applied to the ^{13}C and ^{19}F channels, followed by a free evolution period of fixed duration τ_k.

All experiments are conducted on a Bruker Avance III 400 MHz spectrometer at room temperature. The experimental procedure begins with the preparation of a thermal equilibrium state, followed by pseudo-pure state (PPS) initialization using the selective-transition approach.[48] The resulting PPS is given by $\hat{\rho}_{\text{pps}} = \frac{1-\epsilon}{16} I^{\otimes 4} + \epsilon |0\rangle\langle 0|^{\otimes 4}$ with thermal polarization $\epsilon \approx 10^{-5}$. The fidelity of the prepared PPS is experimentally verified to be approximately 99.71% (see Appendix B for details). For GHZ state preparation, we implement the ACE protocol with a sparse pulse sequence to generate the target state $|\text{GHZ}\rangle = \frac{1}{\sqrt{2}}(|0000\rangle + |1111\rangle)$.

The control sequences are optimized using the L-BFGS-B algorithm[45] starting from random initial parameters. The experimental parameters are set as follows: elementary control pulse duration $\delta t = 20$ μs, free evolution period $\tau_k = 0.48$ ms, and total number of control–evolution layers $K = 30$. This configuration yields a total of $30 \times 4 = 120$ control parameters. For direct comparison, the GRAPE algorithm is configured with $M = 750$ time slices, corresponding to $750 \times 4 = 3000$ parameters, under the same total evolution time $T = 15$ ms.

As shown in Fig. 3(a), the experimental fidelity of the prepared GHZ state, determined through full quantum state tomography, reaches 99.52% for the ACE protocol. Under identical experimental conditions, the GRAPE algorithm achieves a fidelity of 98.05%. Figure 3(b) presents the optimized pulse sequences for both ACE and GRAPE approaches used in the experiment, showing the difference between the sparse pulse sequence and the dense pulse sequence. These experimental results further confirm the numerical results and demonstrate the superior performance of the ACE protocol in terms of both efficiency and robustness.

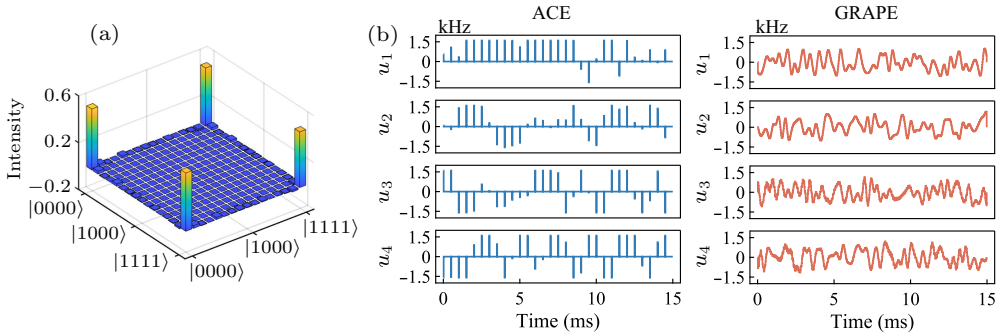


Fig. 3. Experimental performance of the ACE protocol for GHZ state preparation on a 4-qubit NMR quantum system. (a) Experimentally reconstructed density matrix (real part) of the prepared GHZ state using the ACE protocol on the 4-qubit NMR system (^{13}C-iodotriuroethylene, see Appendix B). The imaginary part is negligible (< 0.02). (b) The optimized pulse sequences for GHZ state preparation produced by the ACE protocol (left) and the GRAPE algorithm (right) for the same total evolution time $T = 15$ ms.

5. Discussion and conclusion

In conclusion, we have introduced the alternating control–evolution (ACE) protocol for quantum optimal control. The ACE protocol provides a flexible framework that constructs control sequences by interleaving control pulse slices with tunable free evolutions. By exploiting the intrinsic system dynamics, the ACE protocol enables the design of sparse pulse sequences with a reduced number of control parameters while maintaining high control fidelity. Experimental results demonstrate that the sparse design achieves high-fidelity state preparation with fewer control parameters and exhibits enhanced robustness against control-field noise compared to conventional approaches. To further enhance performance and address more complex tasks,[49,50] the ACE protocol could be integrated with advanced optimization strategies, such as tailored cost function design.[51] Moreover, the ACE protocol can be applied to a wide range of applications, including machine learning tasks,[52,53] unitary operation compilation, and non-unitary control in dissipative systems. In this work, we have focused on closed quantum systems, where the dynamics are governed by the Schrödinger equation and evolution is unitary. However, real systems such as the non-Markovian cases[54–56] are often subject to external environments that induce dissipation and decoherence, and the dynamics become non-unitary, requiring a reformulation of the master equation. For such open quantum systems, the evolution equation and the corresponding cost function would need to be modified to include non-unitary channels.[57,58] Furthermore, additional terms accounting for environmental effects, including dissipation and decoherence, could be incorporated into the cost function. These modifications are compatible with our current protocol and can be directly integrated. Overall, the ACE protocol provides an effective and experimentally robust tool for quantum control, particularly important for near-term quantum devices where parameter efficiency and robustness are essential.

Appendix A: Optimization process of the protocol

In this paper, we utilize the L-BFGS-B optimization approach[45] to find the optimized control sequences in both

the ACE protocol and the GRAPE algorithm. All numerical simulations were performed on a desktop workstation equipped with an Intel® Core™ CPU i7–12700K operating at 3.6 GHz. All numerical examples for state preparation achieved at least a fidelity of 99.7%. Detailed parameters for the nuclear magnetic resonance (NMR) systems of varying sizes will be provided in the subsection.

The pseudocode for the ACE protocol, as described in the preceding text, can be found in Algorithm 1. Let $\tau_k = 0$, we obtain the conventional GRAPE algorithm.

Algorithm 1 The Alternating control-evolution protocol

Input: Target state $|\Psi\rangle$, initial state $|\psi_{\text{in}}\rangle$

Set tolerance ϵ_1, ϵ_2

Output: Optimized parameters $(\boldsymbol{u}^*, \boldsymbol{\tau}^*)$

Initialization: guess control parameters $u_{\alpha,k}^{(0)}$ and evolution durations $\tau_k^{(0)}$ for each layer $k = 1, \ldots, K$

Set $p_1 = 0$, fixed $\boldsymbol{\tau} = \boldsymbol{\tau}^{(0)}$ ▷ Step 1: Optimize control parameters with fixed evolution durations

while $L(\boldsymbol{u}^{(p_1)}, \boldsymbol{\tau}) \geq \epsilon_1$ **do**

  for each layer $k = 1$ to K **do**

    Construct control propagator $U_k^{(p_1)}$ and free-evolution propagator V_k using Eq. (5) and Eq. (6) with parameters $u_{\alpha,k}^{(p_1)}, \tau_k$

  end for

  Calculate the final state: $\left|\psi_{\text{out}}^{(p_1)}\right\rangle = V_K U_K^{(p_1)} \cdots V_1 U_1^{(p_1)} |\psi_{\text{in}}\rangle$

  Calculate the cost function: $L^{(p_1)} = 1 - \left|\langle\Psi| \psi_{\text{out}}^{(p_1)}\rangle\right|^2$

  for each layer $k = 1$ to K and each control direction α **do**

    Calculate gradient $\frac{\partial L^{(p_1)}}{\partial u_{\alpha,k}^{(p_1)}}$ using Eq. (10)

  end for

  for each layer $k = 1$ to K and each control direction α **do**

    Update: $u_{\alpha,k}^{(p_1+1)} \leftarrow u_{\alpha,k}^{(p_1)} - \gamma_1 \frac{\partial L^{(p_1)}}{\partial u_{\alpha,k}^{(p_1)}}$

  end for

  $p_1 \leftarrow p_1 + 1$

end while

Set $p_2 = 0$, initial controls $\boldsymbol{u}^{(0)} = \boldsymbol{u}^{(p_1)}$, initial evolution durations $\boldsymbol{\tau}^{(0)} = \boldsymbol{\tau}$ ▷ Step 2: Simultaneous fine-tuning in constrained region

while $L(\boldsymbol{u}^{(p_2)}, \boldsymbol{\tau}^{(p_2)}) \geq \epsilon_2$ **do**

  Calculate the final state: $\left|\psi_{\text{out}}^{(p_2)}\right\rangle = V_K^{(p_2)} U_K^{(p_2)} \cdots V_1^{(p_2)} U_1^{(p_2)} |\psi_{\text{in}}\rangle$

  Calculate the cost function $L^{(p_2)}$ using current parameters $(\boldsymbol{u}^{(p_2)}, \boldsymbol{\tau}^{(p_2)})$

  Calculate all gradients: $\frac{\partial L^{(p_2)}}{\partial u_{\alpha,k}^{(p_2)}}$ and $\frac{\partial L^{(p_2)}}{\partial \tau_k^{(p_2)}}$

  Update control parameters: $u_{\alpha,k}^{(p_2+1)} \leftarrow u_{\alpha,k}^{(p_2)} - \gamma_2 \frac{\partial L^{(p_2)}}{\partial u_{\alpha,k}^{(p_2)}}$, $\tau_k^{(p_2+1)} \leftarrow \tau_k^{(p_2)} - \gamma_2 \frac{\partial L^{(p_2)}}{\partial \tau_k^{(p_2)}}$

  $p_2 \leftarrow p_2 + 1$

end while

The final parameters: $u_{\alpha,k}^* = u_{\alpha,k}^{(p_2)}$, $\tau_k^* = \tau_k^{(p_2)}$

Return optimized parameters: $(\boldsymbol{u}^*, \boldsymbol{\tau}^*)$

Appendix B: Parameter settings for NMR quantum systems

The nuclear magnetic resonance (NMR) samples employed in the main text are presented in Table B1, with their respective molecular formulas, system sizes (qubit counts), and key spectroscopic parameters. Each sample provides a unique multi-qubit testbed with precession frequencies ν_j and J-coupling networks J_{ij} that define the system Hamiltonian. In our practical optimization, we use a rotating frame to simplify computations. Specifically, we select a reference frequency offset o, and the precession frequency ν we used is defined as $\nu = \omega - o$, where ω is the laboratory-frame Larmor frequency.

In NMR systems, the control field Hamiltonian for the

k-th layer can be written as

$$H_{\mathrm{ctrl},k} = \sum_{j=1}^{n} \left(\pi u_{2j-1,k} \hat{\sigma}_x^{(j)} + \pi u_{2j,k} \hat{\sigma}_y^{(j)} \right). \tag{B1}$$

The gradient components of the ACE protocol are computed as

$$\begin{aligned}
\frac{\partial L}{\partial u_{2j-1,k}} &= 2\,\mathrm{Re}(\lambda \langle \Psi | \mathrm{i}\pi\delta t \cdot U_{\mathrm{left}} V_k \hat{\sigma}_x^{(j)} U_k U'_{\mathrm{right}} | \psi_{\mathrm{in}} \rangle), \\
\frac{\partial L}{\partial u_{2j,k}} &= 2\,\mathrm{Re}(\lambda \langle \Psi | \mathrm{i}\pi\delta t \cdot U_{\mathrm{left}} V_k \hat{\sigma}_y^{(j)} U_k U'_{\mathrm{right}} | \psi_{\mathrm{in}} \rangle), \\
\frac{\partial L}{\partial \tau_k} &= 2\,\mathrm{Re}(\lambda \langle \Psi | \mathrm{i} \cdot U_{\mathrm{left}} H_{\mathrm{NMR}} U_{\mathrm{right}} | \psi_{\mathrm{in}} \rangle),
\end{aligned} \tag{B2}$$

where

$$\begin{aligned}
U_k &= \exp\left[-\mathrm{i} \left(H_{\mathrm{NMR}} + H_{\mathrm{ctrl},k} \right) \delta t \right], \\
V_k &= \exp\left(-\mathrm{i} H_{\mathrm{NMR}} \tau_k \right).
\end{aligned} \tag{B3}$$

The coefficients λ and the left and right operators U_{left}, U_{right}, U'_{right} are expressed in Eqs. (11) and (12).

In the expressibility tests conducted in the main text, we observed a notable increase in the number of layers needed to reach a KL divergence of 10^{-4} in the 7-qubit case. This is primarily attributed to the weaker Hamiltonian couplings present in the crotonic acid sample (see Table B1). Therefore, the sample requires more layers to achieve the desired expressibility.

In the GRAPE algorithm, the number of elementary control slices and the total evolution time T for each system size were empirically determined. Then, under the identical total evolution time T, appropriate free-evolution durations τ_k and number of alternating control–evolution layers K were selected for each system size in the ACE protocol. The parameters of the control sequences constructed by both the ACE protocol and the GRAPE algorithm for each system size mentioned in the journal text can be found in Table B2. In the benchmarking presented, the free-evolution duration in each layer is fixed as $\tau_k = \tau$. The control amplitude $u_{\alpha,k}$ is constrained to the range $[-u_m, u_m]$ for the optimizer. For the practical simulation, u_m is set as follows: 2×10^3 Hz for the 2-qubit case in the GRAPE algorithm; 3×10^4 Hz for the 7-qubit case in the ACE protocol; and 6×10^3 Hz for the remaining cases in both the GRAPE algorithm and the ACE protocol. Additionally, the total evolution time T was much shorter than the system's relaxation time, thus allowing the entire preparation process to be considered unitary.

Table B1. NMR samples of different system sizes. The molecular parameters of each sample including ν_j (diagonal) and J_{ij} (off-diagonal).

Sample name	Molecular formula	System size	Parameters (Hz)
Diethyl fluoromalonate	$FCH(COOC_2H_5)_2$	2 qubits	

	H	F	T_1(s)	T_2 (s)
H	0		2.8	1.2
F	47.6	0	3.1	1.3

Diethyl fluoromalonate — $FCH(COOC_2H_5)_2$ — 3 qubits

	C	H	F	T_1(s)	T_2 (s)
C	0			2.9	1.1
H	160.7	0		2.8	1.2
F	–194.4	47.6	0	3.1	1.3

Carbon-13-iodotrifluroethylene — C_2F_3I — 4 qubits

	C	F_1	F_2	F_3	T_1 (s)	T_2 (s)
C	–20				7.9	1.22
F_1	–297.71	11827			6.8	0.66
F_2	–275.56	64.74	2280		4.4	0.63
F_3	39.17	51.50	–129.08	–11485	4.8	0.61

1-bromo-2,4,5-trifluorobenzene — $BrC_6H_2F_3$ — 5 qubits

	F_1	F_2	F_3	H_1	H_2	T_1 (s)	T_2^* (ms)
F_1	–2451					0.8	50
F_2	–45.5	0				0.6	50
F_3	135.8	323.5	7523			0.8	50
H_1	62.1	1468.2	1811.2	3		1.5	110
H_2	1781.1	122.9	60.9	–10.1	0	1.5	110

Crotonic acid — $C_4H_6O_2$ — 7 qubits

	C_1	C_2	C_3	C_4	H_1	H_2	H_3
C_1	–13249.2						
C_2	40.8	–67					
C_3	1.6	69.5	–2797.1				
C_4	8.47	1.4	71.04	2175.3			
H_1	4.0	155.6	–1.8	6.5	–3.8		
H_2	6.64	–0.7	162.9	3.3	15.81	–469.1	
H_3	128	–7.1	6.6	–0.9	6.9	–1.7	–2071.4

Table B2. Control sequences details of states preparation on NMR quantum systems.

Number of qubits	ACE evolution durations (ms)	ACE control–evolution layers	GRAPE control pulse slices	Total evolution time (ms)
2	0.9800	10	500	10
3	0.5800	20	600	12
4	0.4800	30	750	15
5	0.4600	50	1200	24
7	0.5375	100	2700	54

The pseudopure state (PPS) $\hat{\rho}_{\rm pps}$, prepared from the thermal equilibrium state $\rho_{\rm eq}$ via the selective-transition approach,[48] serves as the initial state for all quantum control experiments. Figure B1(a) displays the characteristic ^{13}C spectrum of the PPS. The target GHZ state was generated using sparse pulse sequences obtained through our ACE protocol, with its readout spectrum after a rotation of $R_y(\pi/2)$ on ^{13}C shown in Fig. B1(b). Full quantum state tomography was performed to characterize the prepared states. For the experimental state fidelities with PPS, we initially obtain $\hat{\rho}$ for the PPS through state tomography, where $\hat{\rho}_{\rm pps} = (1-\epsilon)I/16 + \epsilon\hat{\rho}$. To account for the small polarization factor ϵ, we use the result of the PPS state preparation experiment as a standard reference. All other experimental results are then normalized using this reference value, which allows for the estimation of the density matrix $\hat{\rho}$. The fidelity between the target pure state $|\psi\rangle = |0000\rangle$ and the experimental $\hat{\rho}$ is quantified as $F(|\psi\rangle, \hat{\rho}) = \langle\psi|\hat{\rho}|\psi\rangle$. The resulting reconstructed density matrices for the PPS and GHZ state are shown in Figs. B1(c) and B1(d). The reconstructed PPS achieved a fidelity of 99.71%, while the GHZ state reached 99.52% fidelity, demonstrating the high precision of our protocol for state preparation. Ideal results are provided in Figs. B1(e) and B1(f) for comparison.

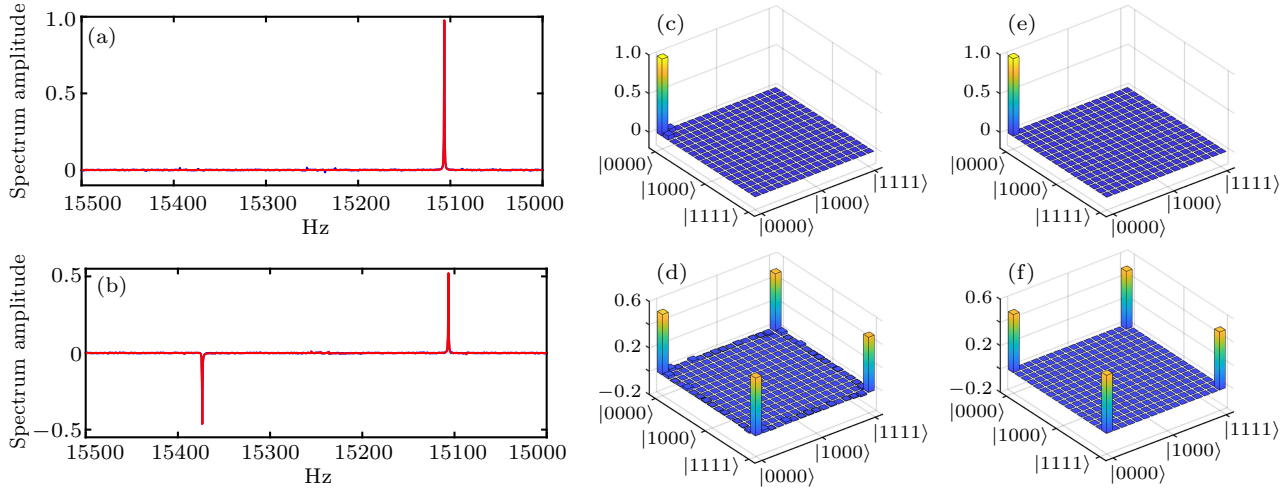


Fig. B1. Experimental data and the corresponding tomography results. (a) Experimental ^{13}C spectra of PPS ρ_{0000} state and (b) GHZ state with $R_y(\pi/2)$ rotation on ^{13}C as the readout operator. (c) The tomography results of experimentally reconstructed density matrix (real part) of the prepared PPS state and (d) the prepared GHZ state. The imaginary part is negligible (< 0.02). (e) The ideal density matrix (real part) of the PPS state and (f) the GHZ state.

Acknowledgements

This work is supported by Quantum Science and Technology — National Science and Technology Major Project of China (Grant Nos. 2024ZD0302000 and 2021ZD0303205), the National Natural Science Foundation of China (Grant Nos. 92165108, 12261160569, 12150014, and 11927811), and the XPLORER Prize.

References

[1] Glaser S J, Boscain U, Calarco T, Koch C P, Köckenberger W, Kosloff R, Kuprov I, Luy B, Schirmer S, Schulte-Herbrüggen T, Sugny D and Wilhelm F K 2015 *Eur. Phys. J. D* **69** 279

[2] Waldherr G, Wang Y, Zaiser S, Jamali M, Schulte-Herbrüggen T, Abe H, Ohshima T, Isoya J, Du J F, Neumann P and Wrachtrup J 2014 *Nature* **506** 204

[3] Dolde F, Bergholm V, Wang Y, Jakobi I, Naydenov B, Pezzagna S, Meijer J, Jelezko F, Neumann P, Schulte-Herbrüggen T, Biamonte J and Wrachtrup J 2014 *Nat. Commun.* **5** 3371

[4] Krotov V F 1993 *Advances in Nonlinear Dynamics and Control: A Report from Russia* (Boston, MA: Birkhäuser Boston) pp. 74–121

[5] Bryson A E 1975 *Applied Optimal Control: Optimization, Estimation and Control* (1st edn.) (New York: Routledge)

[6] D'Alessandro D 2021 *Introduction to Quantum Control and Dynamics* (2nd edn.) (New York: Chapman and Hall/CRC)

[7] Machnes S, Assémat E, Tannor D and Wilhelm F K 2018 *Phys. Rev. Lett.* **120** 150401

[8] Liebermann P J and Wilhelm F K 2016 *Phys. Rev. Appl.* **6** 024022

[9] Egger D J and Wilhelm F K 2014 *Phys. Rev. Lett.* **112** 240503

[10] Khaneja N, Reiss T, Kehlet C, Schulte-Herbrüggen T and Glaser S J 2005 *J. Magn. Reson.* **172** 296

[11] August M and Hernández-Lobato J M 2018 *High Performance Computing* (Cham: Springer International Publishing) pp. 591–613

[12] Ge X, Ding H, Rabitz H and Wu R B 2020 *Phys. Rev. A* **101** 052317

[13] Ge X and Wu R B 2021 *Phys. Rev. A* **104** 012422

[14] Turinici G 2019 *Phys. Rev. A* **100** 053403

[15] Morzhin O V and Pechen A N 2019 *Russ. Math. Surv.* **74** 851
[16] Fernandes M E F, Fanchini F F, de Lima E F and Castelano L K 2023 *J. Phys. A: Math. Theor.* **56** 495303
[17] Caneva T, Calarco T and Montangero S 2011 *Phys. Rev. A* **84** 022326
[18] Rach N, Müller M M, Calarco T and Montangero S 2015 *Phys. Rev. A* **92** 062343
[19] Zhiyenbayev Y, Akulin V M and Mandilara A 2018 *Phys. Rev. A* **98** 012325
[20] Kwon S, Tomonaga A, Bhai G L, Devitt S J and Tsai J S 2021 *J. Appl. Phys.* **129** 041102
[21] Boutin S, Andersen C K, Venkatraman J, Ferris A J and Blais A 2017 *Phys. Rev. A* **96** 042315
[22] Dalgaard M, Motzoi F, Jensen J H M and Sherson J 2020 *Phys. Rev. A* **102** 042612
[23] Saywell J, Carey M, Belal M, Kuprov I and Freegarde T 2020 *J. Phys. B: At. Mol. Opt. Phys.* **53** 085006
[24] Katz O, Cetina M and Monroe C 2023 *PRX Quantum* **4** 030311
[25] Yang X D, Arenz C, Pelczer I, Chen Q M, Wu R B, Peng X H and Rabitz H 2020 *Phys. Rev. A* **102** 062605
[26] Li S Y, Fan Y D, Li X, Ruan X H, Zhao Q C, Peng Z H, Wu R B, Zhang J and Song P T 2025 *npj Quantum Inf.* **11** 124
[27] Kim L, Lloyd S and Marvian M 2024 *Phys. Rev. Res.* **6** 033019
[28] Guo L L, Duan P, Zhang S, Yang X X, Zhang C, Du L, Zhang H F, Tao H R, Wang T L, Jia Z L, Chen Z Y and Guo G P 2024 *Phys. Rev. Appl.* **21** 064060
[29] Undseth B, Pietx-Casas O, Raymenants E, Mehmandoost M, Mądzik M T, Philips S G J, de Snoo S L, Michalak D J, Amitonov S V, Tryputen L, Wuetz B P, Fezzi V, Esposti D D, Sammak A, Scappucci G and Vandersypen L M K 2023 *Phys. Rev. X* **13** 041015
[30] Liu R, Yang X, Lin Y, Lu Y, Li J 2025 *Chin. Phys. Lett.* **42** 080601
[31] Bruzewicz C D, Chiaverini J, McConnell R and Sage J M 2019 *Appl. Phys. Rev.* **6** 021314
[32] Levine H, Keesling A, Omran A, Bernien H, Schwartz S, Zibrov A S, Endres M, Greiner M, Vuletić V and Lukin M D 2018 *Phys. Rev. Lett.* **121** 123603
[33] Krantz P, Kjaergaard M, Yan F, Orlando T P, Gustavsson S and Oliver W D 2019 *Appl. Phys. Rev.* **6** 021318
[34] Rong X, Geng J P, Shi F Z, Liu Y, Xu K B, Ma W C, Kong F, Jiang Z, Wu Y and Du J F 2015 *Nat. Commun.* **6** 8748
[35] Dobrovitski V V, Fuchs G D, Falk A L, Santori C and Awschalom D D 2013 *Annu. Rev. Condens. Matter Phys.* **4** 23
[36] Pan J, Yu Q and Peng X H 2017 *Acta Phys. Sin.* **66** 150302 (in Chinese)
[37] Correr G I, Medina I, Azado P C, Drinko A and Soares-Pinto D O 2024 *Quantum Sci. Technol.* **10** 015008
[38] Chen C C, Watabe M, Shiba K, Sogabe M, Sakamoto K and Sogabe T 2021 *ACM Trans. Quantum Comput.* **2** 8
[39] Liu Y, Kaneko K, Baba K, Koyama J, Kimura K and Takeda N 2025 *IEEE Trans. Quantum Eng.* **6** 1
[40] Nakata Y, Koashi M and Murao M 2014 *New J. Phys.* **16** 053043
[41] Sim S, Johnson P D and Aspuru-Guzik A 2019 *Adv. Quantum Technol.* **2** 1900070
[42] Życzkowski K and Sommers H J 2005 *Phys. Rev. A* **71** 032313
[43] Møllersen K, Dhar S and Godtliebsen F 2016 *Appl. Math.* **7** 1674
[44] Mele A A 2024 *Quantum* **8** 1340
[45] Byrd R H, Lu P, Nocedal J and Zhu C 1995 *SIAM J. Sci. Comput.* **16** 1190
[46] Li J, Fan R H, Wang H Y, Ye B T, Zeng B, Zhai H, Peng X H and Du J F 2017 *Phys. Rev. X* **7** 031011
[47] Chen X, Wu Z, Jiang M, Lü X Y, Peng X H and Du J F 2021 *Nat. Commun.* **12** 6281
[48] Peng X H, Zhu X W, Fang X M, Feng M, Gao K L, Yang X D and Liu M L 2001 *Chem. Phys. Lett.* **340** 509
[49] Cerezo M, Sone A, Volkoff T, Cincio L and Coles P J 2021 *Nat. Commun.* **12** 1791
[50] Arenz C and Rabitz H 2020 *Phys. Rev. A* **102** 042207
[51] Wang X M, Yang C R and Gu M 2024 *Phys. Rev. Lett.* **133** 130602
[52] Li W K, Lu Z D and Deng D L 2022 *SciPost Phys. Lect. Notes* 61
[53] Bondarenko D and Feldmann P 2020 *Phys. Rev. Lett.* **124** 130502
[54] Shen H Z, Wang Q, Wang J and Yi X X 2020 *Phys. Rev. A* **101** 013826
[55] Shen H Z, Shang C, Zhou Y H, and Yi X X 2018 *Phys. Rev. A* **98** 023856
[56] Shen H Z, Yang J F and Yi X X 2024 *Phys. Rev. A* **109** 043714
[57] Breuer H P, Laine E M and Piilo J 2009 *Phys. Rev. Lett.* **103** 210401
[58] Vacchini B and Breuer H P 2010 *Phys. Rev. A* **81** 042103